

# Fast gas heating of nanosecond pulsed surface dielectric barrier discharge: spatial distribution and fractional contribution from kinetics

Yifei Zhu  and Svetlana Starikovskaia<sup>1</sup>

Laboratory of Plasma Physics (CNRS, Ecole Polytechnique, UPMC, Univ. Paris-Sud, Observatoire de Paris, Paris-Saclay University, Sorbonne Universities), Ecole Polytechnique, route de Saclay, 91128 Palaiseau, France

E-mail: [yifei.zhu@lpp.polytechnique.fr](mailto:yifei.zhu@lpp.polytechnique.fr) and [svetlana.starikovskaya@lpp.polytechnique.fr](mailto:svetlana.starikovskaya@lpp.polytechnique.fr)

Received 8 July 2018, revised 14 November 2018

Accepted for publication 26 November 2018

Published 28 December 2018



CrossMark

## Abstract

The effect of heat release in reactions with charged and electronically excited species, or so-called fast gas heating (FGH), in nanosecond surface dielectric barrier discharge (nSDBD) in atmospheric pressure air is studied. Two-dimensional numerical simulations based on the PARallel Streamer Solver with KinEtics code are conducted. The code is based on the direct coupling of a self-consistent fluid model with detailed kinetics, an efficient photoionization model, and Euler equations. The choice of local field approximation for nSDBD modeling with simplified kinetics is discussed. The reduced electric field and the electron density are examined at both polarities for identical high-voltage pulses 24 kV in amplitude on a high-voltage electrode and 20 ns full width at half maximum. The distribution of the FGH energy and the resulting gas temperature field are studied and compared with findings in the literature. The input of different reactions to the appearance of hydrodynamic perturbations is analyzed.

Keywords: nanosecond surface dielectric barrier discharge, nSDBD, plasma modeling, fast gas heating

## 1. Introduction

Surface dielectric barrier discharge (SDBD) has been studied intensively in recent years due to its potential use in the community of aerodynamics. In an SDBD, the high-voltage electrode ('top electrode', or 'exposed electrode') is placed above the dielectric surface, and the low-voltage, typically grounded or at constant potential, electrode is placed below the dielectric surface [1–4]. At atmospheric pressure, micro-discharges appear stochastically in the vicinity of the high-voltage electrode and develop into streamers propagating along the dielectric surface. The discharge is typically more uniform during the negative half period. The ion wind generating in the discharge produces a gas flow along the dielectric surface. With sinusoidal voltage amplitudes from a

few kV to 20–30 kV and frequencies in the range of 1–10 kHz, SDBDs can generate a flow of a few  $\text{m s}^{-1}$  up to  $10 \text{ ms}^{-1}$ .

In the case where short high-voltage pulses (a voltage pulse can be from units to several tens of kilovolts with rise and decay times on the order of or less than 10 ns) are used to initiate the nanosecond SDBDs (nSDBDs), the streamers start synchronously (within at least 0.2 ns) from the high-voltage electrode and propagate along the dielectric. Starting from early 2000s, nanosecond discharge was studied for plasma-assisted flow control [5–10]. The main mechanism of the flow influence by nSDBD is a fast and coherent heat release producing a weak shock wave in the vicinity of the exposed electrode. According to [11], transient temperature rise in the nSDBD, produced by input energy thermalization over a wide time scale, is responsible for the generation of shock waves, the low-density regions that may affect the external flow as

<sup>1</sup> Author to whom any correspondence should be addressed.

‘thermal bumps’ and ‘delayed’ stochastic near-surface perturbations. Another possible application of nanosecond surface DBDs is plasma-assisted ignition and combustion. It was demonstrated in [12] that at equal energies deposited in the discharge during the same period the flame from the nSDBD occupies a larger volume than that of the nanosecond spark, and that the flame front initiated by nSDBD moves significantly faster. This has been explained by the interaction of combustion waves initiated by different streamers. Recently, the use of nSDBD for plasma-assisted anti-icing has also increased the interest of researchers [13–15]. All the applications mentioned above are closely related to the fast gas heating (FGH) and temperature characteristics of nSDBD.

FGH is one of the key features of nanosecond discharges. Traditionally, relaxation of energy from charged species and from electronic excitation is understood under FGH in a transient nanosecond plasma. The relaxation occurs at a time scale much less than vibrational-translational relaxation (VT relaxation) or vibrational-vibrational exchange (VV exchange). Recently, it has been experimentally proven that open electrode nanosecond discharges provide significant localized heat release during a short time period: an increase of gas temperature of about 900 K during 20 ns was measured in pin-to-pin 4 mm gap discharge in air preheated to 1000 K [16]. Two phases of gas heating, fast and slow, were distinguished experimentally in pin-to-plane discharge in atmospheric pressure air by means of emission spectroscopy and spontaneous Raman scattering [17]: the first phase, at tens of nanoseconds, corresponded to the relaxation of electronically excited species [18]; and the second one, at tens and hundreds of microseconds, was explained by VT relaxation. Measurements of gas temperature in the vicinity of the high-voltage electrode (1 mm large zone) of the atmospheric pressure nSDBD [19] agree with the conclusions made in [17]. The measured gas temperature was equal to 340–380 K for the discharge period, and 380–460 K in the afterglow, at  $t \sim 1 \mu\text{s}$ . The effects of FGH have also been studied and validated numerically. Calculations of the dynamics of formation of a nanosecond spark discharge between two point electrodes in air at atmospheric pressure at 300 and 1000 K were carried out in [20–22]. It was shown that a 10 ns spark discharge significantly heats ambient air on a time scale of tens of nanoseconds. The mechanism of FGH in a pin-plane atmospheric pressure streamer discharge and the effects of humidity were discussed in [23, 24] on the basis of numerical modeling. It was concluded that in humid air, rapid vibration-to-translation transitions of  $\text{H}_2\text{O}$  and the exothermicity of the reactions of OH formation additionally increase the gas temperature.

Despite the progress made in the analysis of FGH, only a few works suggesting the detailed kinetics of FGH in nSDBD are available. Two main kinetic schemes validated by experiments have been developed and used to study the features of FGH by different groups [18, 25]. A good agreement between calculations and experiments confirms that energy relaxation from the electronic degrees of freedom of excited species is the heating source at a time scale much less than that of VT relaxation, or VV exchange. Two key parameters

can be defined to characterize FGH in nanosecond pulsed discharge, the fractional power of each process related to total FGH power  $\eta_{\text{proc}}$  and the fractional power of FGH related to total electron power  $\eta_{\text{total}}$ . The first parameter,  $\eta_{\text{proc}}$ , was used to evaluate the contribution of each process to FGH. Reference [18] concluded that for the  $E/N$  ranging from 150–900 Td, FGH in air results mainly from the dissociation of nitrogen and oxygen molecules, quenching of the electronically excited states of nitrogen molecules and excited atoms  $\text{O}({}^1\text{D})$  and reactions of electron–ion and ion–ion recombination. The fraction of energy released through different channels is a function of the reduced electric field. The contribution of different processes to FGH was calculated in [18] for air at pressure 760 Torr. At fields  $E/N \leq 200\text{--}300$  Td the dominant processes are quenching of  $\text{N}_2(\text{C}^3\Pi_u)$  and  $\text{N}_2(\text{B}^3\Pi_g)$  states by molecular oxygen and quenching of  $\text{O}({}^1\text{D})$  atoms, with a total contribution of more than 70%. At high reduced electric fields ionization becomes sufficient, and the heating due to charged particles becomes dominant. The second parameter,  $\eta_{\text{total}}$ , is more practical for applications as it can be directly used to estimate FGH on the basis of measured or calculated deposited energy. At high electric fields, there is discussion on the value of  $\eta_{\text{total}}$ . The authors of [25] concluded that  $\eta_{\text{total}}$  increases with  $E/N$ , and can reach 50%–60% at  $E/N \geq 1000$  Td. In [18]  $\eta_{\text{total}}$  does not exceed  $30\% \pm 3$ . The difference is caused by different treatment of energy release from electron–ion recombination reactions.

The aim of this work is to study the FGH produced by nSDBD by numerical simulation with the support of experimental facts. With a set of detailed kinetics, the fractional contribution from the main processes to total FGH energy release is analyzed for the discharge of both polarities. The temperature distribution and evolution near the electrode edge and in the streamer channel and the main processes responsible for FGH are discussed.

## 2. Model description

This paper is a continuation of a previous study [26], which focused on the detailed structure and dynamics of nSDBD. The experimental conditions are similar, and the numerical code developed in [26] is used. In this section, the kinetics scheme concerning FGH, and the use of local field approximation (LFA) for FGH calculation are discussed in detail.

### 2.1. Governing equations

A general scheme of the experimental geometry and applied voltage pulses are given in figures 1(a) and (b). Two electrodes (orange) with thicknesses of  $50 \mu\text{m}$  are separated by a PVC dielectric layer with a thickness of 0.3 mm and dielectric permittivity equal to 4. The voltage pulses of 24 kV of both polarities, 2 ns the rise time, and 20 ns full width at half maximum (FWHM), were applied to the high-voltage electrode. The details of the experimental setup can be found in [26].

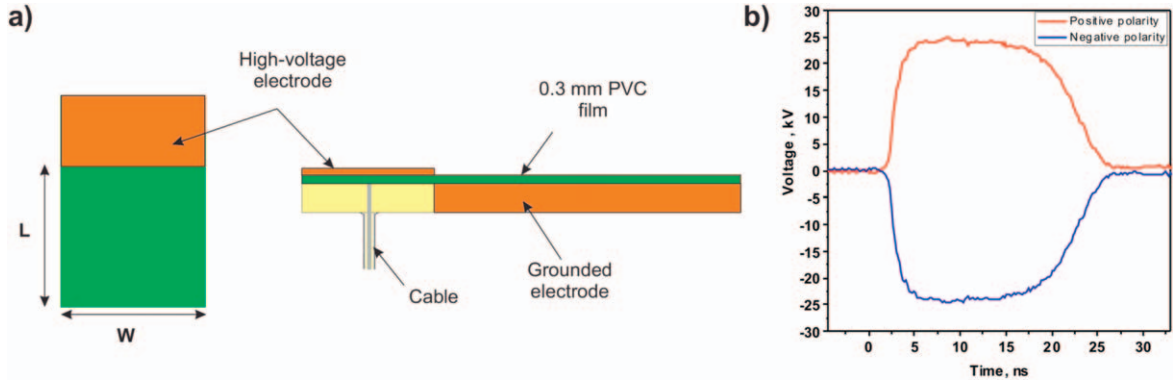


**Figure 1.** General scheme of the experimental geometry (a) and applied voltage pulses in both polarities (b).

The parallel code, PASSKEY (PARallel Streamer Solver with KinEtics), is used in this work. The numerical approaches, with respect to the code validation on two benchmarks cases and comparison with experiments, are presented in detail in [26]. The first moment of the Boltzmann equation for the charged species is described by the PASSKEY code assuming that neutral species do not move in the time scale of nanoseconds:

$$\frac{\partial n_i}{\partial t} - \nabla \cdot \mathbf{\Gamma}_i = S_i + S_{ph}, \quad i = 1, 2, \dots, N_{total} \quad (1)$$

$$\mathbf{\Gamma}_i = D_i \nabla n_i + (q_i/|q_i|) \mu_i n_i \nabla \Phi, \quad i = 1, 2, \dots, N_{charge}, \quad (2)$$

where  $\Phi$  is the electrical potential, and  $n_i$ ,  $q_i$ , and  $S_i$  are the number density, charge, and source function for species  $i$ , respectively. The source function  $S_i$  includes gain and loss terms due to gas phase reactions, and  $S_{ph}$  is the photoionization source term for electrons and oxygen ions.  $D_i$  and  $\mu_i$  are the diffusion coefficient and mobility of charged species, respectively. In the code,  $\nabla \cdot \mathbf{j} = 0$  for neutral species is postulated.  $N_{charge}$  and  $N_{neutral}$  are the number density of the total species, charged species, and neutral species, respectively. The chemical source term  $S$  is calculated with detailed kinetics.

The photoionization model [27] describing the ionization of oxygen molecules by vacuum ultraviolet (VUV) radiation coming from electronically excited  $N_2$  in  $b^1\Pi_u$ ,  $b^1\Sigma_u^+$ ,  $c^1\Sigma_u^+$  states is considered. The model is based on the assumption that the major contribution to the rate of photoionization comes from the radiation in the spectral range 98–102.5 nm; the radiation below 98 nm is absorbed by molecular nitrogen, and the wavelength of 102.5 nm is the photoionization threshold of  $O_2$ . The photoionization source term  $S_{ph}$  is calculated by introducing three terms Helmholtz equations [28, 29]:

$$S_{ph} = \sum_j S_{ph}^j, \quad (3)$$

$$\nabla^2 S_{ph}^j - (\lambda_j p_{O_2})^2 S_{ph}^j = -A_j p_{O_2}^2 I, \quad (4)$$

$$I = \xi \frac{p_q}{p + p_q} \alpha \mu E n_e, \quad (5)$$

where  $\alpha$  is the Townsend ionization coefficient,  $\mu E$  is the absolute drift velocity of electrons,  $p$  is the ambient pressure,

$p_q$  is the quenching pressure of  $C^3\Pi_u$ , and  $p_{O_2}$  is the partial pressure of  $O_2$ .  $\lambda_j$  and  $A_j$  are the fitting coefficients for the photoionization functions obtained in experiments and taken from [28]. The quenching pressure is expressed as  $p_q = kT/\tau_0 k_q$ , where  $k$  is the Boltzmann constant,  $T$  is the gas temperature, and  $\tau_0$  and  $k_q$  are the radiative lifetime of the transition and the rate constant of collisional quenching, respectively.

Poisson's equation is solved without taking into account the current in the material:

$$\nabla(\epsilon \nabla \Phi) = -\sum_{i=1}^{N_{ch}} q_i n_i - \rho, \quad (6)$$

where  $\rho$  is the charge density satisfying continuity equations for charges on surfaces:

$$\frac{\partial \rho}{\partial t} = \sum_{j=1}^n q_j [-\nabla \cdot \mathbf{\Gamma}_j + S_j]. \quad (7)$$

Finally, the system of equations is added with the Euler equations:

$$\frac{\partial \mathbf{U}}{\partial t} + \frac{\partial \mathbf{F}}{\partial x} + \frac{\partial \mathbf{G}}{\partial y} = \mathbf{S} \quad (8)$$

$$\mathbf{U} = \begin{bmatrix} \rho \\ \rho u \\ \rho v \\ e \end{bmatrix}, \quad \mathbf{F} = \begin{bmatrix} \rho u \\ p + \rho u u \\ \rho u v \\ (e + p)u \end{bmatrix}, \quad \mathbf{G} = \begin{bmatrix} \rho v \\ \rho u v \\ p + \rho v v \\ (e + p)v \end{bmatrix}, \quad \mathbf{S} = \begin{bmatrix} 0 \\ 0 \\ 0 \\ S_{heat} \end{bmatrix}, \quad (9)$$

where  $\rho$  is the total density of air,  $u$  and  $v$  are the velocities in two dimensions, and  $e$  is the specific total energy. The reactive Euler equations are closed by the equation of state:

$$p = (\gamma - 1) \rho i, \quad (10)$$

where  $i = e - (u^2 + v^2)/2$  is the specific internal energy.

The energy, released in FGH and calculated from kinetics equations in the plasma code is used as the source term in equation (9). The calculated density, pressure, and temperature from the Euler equations are further used for  $E/N$  calculation, Helmholtz equations, and kinetics.

**Table 1.** Kinetics scheme for nSDBD considering FGH.

No.	Reaction	Rate constant <sup>a</sup>	Ref.
R1	$e + N_2 \rightarrow e + e + N_2^+$	$f(\sigma, E/N)$	[32]
R2	$e + O_2 \rightarrow e + e + O_2^+$	$f(\sigma, E/N)$	[33]
R3	$e + N_2 \rightarrow e + N_2(A^3\Sigma_u)$	$f(\sigma, E/N)$	[32]
R4	$e + N_2 \rightarrow e + N_2(B^3\Pi_g)$	$f(\sigma, E/N)$	[32]
R5	$e + N_2 \rightarrow e + N_2(C^3\Pi_u)$	$f(\sigma, E/N)$	[32]
R6	$e + O_2 \rightarrow e + O + O + 0.8 \text{ eV}$	$f(\sigma, E/N)$	[18, 33]
R7	$e + O_2 \rightarrow e + O + O(^1D) + 1.26 \text{ eV}$	$f(\sigma, E/N)$	[18, 33]
R8	$N_2^+ + N_2 + M \rightarrow N_4^+ + M + 1.057 \text{ eV}$	$5 \cdot 10^{-29}$	[18, 30]
R9	$N_4^+ + O_2 \rightarrow O_2^+ + N_2 + N_2 + 2.453 \text{ eV}$	$2.5 \cdot 10^{-10}$	[18, 30]
R10	$N_2^+ + O_2 \rightarrow O_2^+ + N_2 + 3.51 \text{ eV}$	$6 \cdot 10^{-11}$	[18, 30]
R11	$O_2^+ + N_2 + N_2 \rightarrow O_2^+N_2 + N_2$	$9 \cdot 10^{-31}$	[30]
R12	$O_2^+N_2 + N_2 \rightarrow O_2^+ + N_2 + N_2$	$4.3 \cdot 10^{-10}$	[30]
R13	$O_2^+N_2 + O_2 \rightarrow O_4^+ + N_2$	$10^{-9}$	[30]
R14	$O_2^+ + O_2 + M \rightarrow O_4^+ + M + 0.425 \text{ eV}$	$2.4 \cdot 10^{-30}$	[18, 30]
R15	$e + O_2 + O_2 \rightarrow O_2^- + O_2$	$2 \cdot 10^{-29}(300/T_e)$	[30]
R16	$e + O_2 \rightarrow O^- + O$	$f(\sigma, E/N)$	[33]
R17	$O^- + O \rightarrow e + O_2$	$1.4 \cdot 10^{-10}$	[31]
R18	$O_2^- + O \rightarrow e + O_2 + O$	$1.5 \cdot 10^{-10}$	[31]
R19	$e + N_4^+ \rightarrow N_2 + N_2(C^3\Pi_u) + 3.49 \text{ eV}$	$2.3 \cdot 10^{-6}(300/T_e)^{0.53}$	[31]
R20	$e + N_2^+ \rightarrow N + N + 2.25 \text{ eV}$	$1.8 \cdot 10^{-7}(300/T_e)^{0.39}$	[31]
R21	$e + O_4^+ \rightarrow O + O + O_2 + 4.6 \text{ eV}$	$1.4 \cdot 10^{-6}(300/T_e)^{0.50}$	[18, 30]
R22	$e + O_2^+ \rightarrow O + O + 5.0 \text{ eV}$	$2.0 \cdot 10^{-7}(300/T_e)$	[18, 30]
R23	$O_2^- + O_4^+ \rightarrow O_2 + O_2 + O_2 + 6.5 \text{ eV}$	$10^{-7}$	[30]
R24	$O_2^- + O_4^+ + M \rightarrow O_2 + O_2 + O_2 + M + 6.5 \text{ eV}$	$2 \cdot 10^{-25}$	[30]
R25	$O_2^- + O_2^+ + M \rightarrow O_2 + O_2 + M + 7.0 \text{ eV}$	$2 \cdot 10^{-25}$	[30]
R26	$O^- + N_2^+ \rightarrow O + N + N + 2.25 \text{ eV}$	$2.0 \cdot 10^{-7}(300/T_{\text{gas}})^{0.50}$	[34]
R27	$N_2(C^3\Pi_u) + N_2 \rightarrow N_2(B^3\Pi_g, v) + N_2$	$1.0 \cdot 10^{-11}$	[18]
R28	$N_2(C^3\Pi_u) + O_2 \rightarrow N_2 + O + O(^1D) + 4.83 \text{ eV}$	$3.0 \cdot 10^{-10}$	[18]
R29	$N_2(C^3\Pi_u) \rightarrow N_2 + h\nu$	$2.45 \cdot 10^7$	[30]
R30	$N_2(B^3\Pi_g) + O_2 \rightarrow N_2 + O + O + 2.35 \text{ eV}$	$3.0 \cdot 10^{-10}$	[18]
R31	$N_2(B^3\Pi_g) + N_2 \rightarrow N_2(A^3\Sigma_u) + N_2(v)$	$1.0 \cdot 10^{-11}$	[18]
R32	$N_2(A^3\Sigma_u) + O_2 \rightarrow N_2 + O + O + 1.0 \text{ eV}$	$2.5 \cdot 10^{-12}(T_{\text{gas}}/300)^{0.50}$	[18]
R33	$O(^1D) + O_2 \rightarrow O + O_2 + 0.33 \text{ eV}$	$3.3 \cdot 10^{-11} \exp(67/T_{\text{gas}})$	[18]
R34	$O(^1D) + N_2 \rightarrow O + N_2 + 1.37 \text{ eV}$	$1.8 \cdot 10^{-11} \exp(107/T_{\text{gas}})$	[18]

<sup>a</sup> Rate constants are given in  $s^{-1}$ ,  $cm^3 \cdot s^{-1}$ , and  $cm^6 \cdot s^{-1}$ . Electron temperature  $T_e$  is taken as a function of  $E/N$  based on BOLSIG+ with cross sections indicated in the table, units in K. Gas temperature  $T_{\text{gas}}$  is calculated from fluid module in PASSKEY, units in K. The energy release in each reaction is from the work of [18].

## 2.2. Kinetics scheme

In the present work the kinetics scheme from [30] to model streamer propagation, the kinetics of [18] to describe the FGH, and the kinetics of [31] are combined. The following neutral, charged, and excited species are taken into account:  $e$ ,  $N_2$ ,  $N_2(A^3\Sigma_u^+)$ ,  $N_2(B^3\Pi_g)$ ,  $N_2(C^3\Pi_u)$ ,  $N_2^+$ ,  $N_4^+$ ,  $O_2$ ,  $O$ ,  $O(^1D)$ ,  $O_2^+$ ,  $O_4^+$ ,  $O^-$ ,  $O_2^-$ , and  $O_2^+N_2$ . The scheme includes 15 species and 34 reactions. Detailed reactions and corresponding rates are given in table 1. This scheme has been successfully used in [26].

The value of energy released in the electron-ion recombination reaction (R21) is different in different existing sources. In [25] this value is 11.66 eV assuming  $e + O_4^+ \rightarrow O_2 + O_2$ . In [18] the value is taken as 4.6 eV, considering that the binding energy of the  $O_2^+ \cdot O_2$  ion is relatively small (0.42 eV) so the electron-ion recombination

of the  $O_2^+ \cdot O_2$  ion proceeds similarly to that of the  $O_2^+$  ion. In this work the value given in [18] is used in the analysis of the results. A possible influence of this difference is discussed in section 3.1.

It is also important to note that the gas heating related with ions can also be accounted for from ion current  $J_i E$  (especially for the cathode region as ion transport in this region is significant, the heating caused by ion current is even greater than the FGH caused by electrons). To be consistent with the method used in this work, the gas heating for the cathode region is calculated based on the kinetics scheme proposed in table 1, thus the calculated temperature will be underestimated inside the cathode region.

### 2.3. The use of LFA

The electron transport coefficients and rate coefficients are obtained by solving the Boltzmann equation for the electron energy distribution function (EEDF) using the two-term approximation [35]. Once the electron temperature is known, the collision frequency and reaction rate coefficients are determined by interpolating from a Boltzmann-derived lookup table using electron temperature based on local mean energy approximation (LMEA), or electric field based on LFA.

The PASSKEY code used in [26] is based on LFA, meaning that local equilibrium of electrons is achieved instantaneously in response to the electric field. All the transport coefficients and source terms are explicit functions of the norm of the local reduced electric field  $E/N$ . This is the case when the time scales of variations of the electric field and electron density are longer than the time scale of energy relaxation. It must be noted that LFA is not always valid for surface streamers due to the nonlocal effect in the high field regions. The loss of accuracy of LFA in streamer modeling can appear in two regions, the ionization head and streamer bottom above the dielectric surface.

In the ionization head, LFA may lead to underestimation of ionizations. The effects of nonlocality on positive streamers in air at atmospheric pressure were studied in [36], where the corrections for the electron source term rates were calculated in the LFA following the work in [37]. Deviations from the LFA were studied for negative streamers in nitrogen at atmospheric pressure [38] by means of a comparison between 1D fluid and particle models. By taking into account the nonlocal effects, all of these authors found an increase in the ionization in the streamer head, a resulting increase of the electric field and a small increase of the streamer velocity. The discrepancies given by LFA discussed above are far smaller than an order of magnitude. For example, [38] reports a relative difference between the fluid and the particle models of 10%–20% in the ionization level behind the streamer front for homogeneous applied electric fields of 50 and 100 kV cm<sup>-1</sup>, respectively. For practical accuracy, one can obtain the main streamer characteristics by a fluid model [36]. Furthermore, recently in [39] a PIC code was used to solve the Boltzmann equation and a Monte Carlo simulation was used to simulate collisions, in the framework of streamer simulations in the Earth's atmosphere as applicable to sprite discharges. These authors found an excellent agreement with the results obtained by a fluid model in [40] both for positive and negative streamers.

In the near-wall region where plasma is close to the dielectric surface, LFA may lead to overestimation of ionizations. As mentioned in [41], the electrons could move against the E-field force due to the strong diffusion associated with the high concentration gradient and enter into the region of a strong E-field. In this region, the predicted ionization source is high and the electron-ion density increases dramatically. The real ionization source cannot be very high, because the electrons lose their energy moving against the E-field force and cannot ionize gas molecules very effectively. Reference

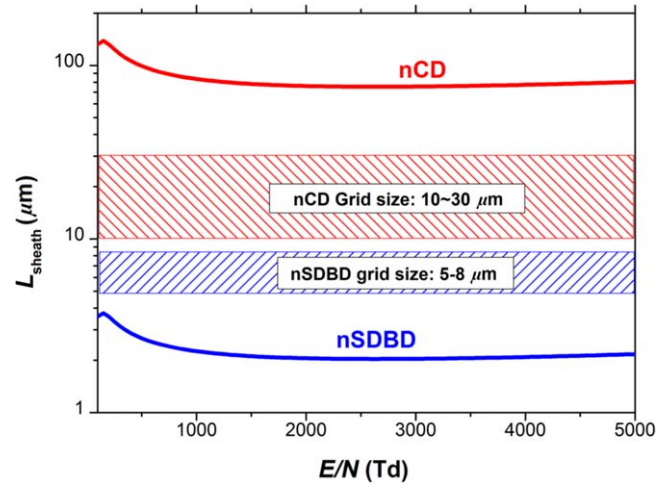


**Figure 2.** The characteristic length of region with the possibility of ‘electron cooling by field’ in nCD and nSDBD modeling. If the mesh grid size is smaller than the line of  $L_{\text{sheath}}$ , LMEA is the best choice for a fluid model of plasma.

[41] used a corrected ionization electron source to overcome this problem.

The aim of this work is to study the energy release in the main channel of the discharge, but not the very thin region between the streamer body and dielectric. To have a quantitative view on the use of LFA, we made a simple estimation based on the effect of ‘electron cooling by field’. Assuming there is a sheath region where the electron density  $n_e$  drops from  $n_{e\text{max}}$  to 0 on the length  $L_{\text{sheath}}$ , and the diffusion flux is larger than convection within this region:

$$D_e \nabla n_e > \mu n_e E. \quad (11)$$

Let  $n_{e\text{avg}}$  be the average electron density within the sheath, assuming the Einstein relationship  $D_e = \mu T_e$ , then the above equation can be simplified as:

$$\mu T_{es} \frac{n_{e\text{max}}}{L_{\text{sheath}}} > \mu E_s n_{e\text{avg}}, \rightarrow L_{\text{sheath}} < \frac{T_{es} n_{e\text{max}}}{E_s n_{e\text{avg}}}, \quad (12)$$

where  $T_{es}$  and  $E_s$  are the electron temperature and electric field in the sheath region. If one considers  $n_{e\text{max}} = 2n_{e\text{avg}}$ , then the length of  $L_{\text{sheath}} < 2T_{es}/E_s$  can be considered as the limit length, below which the behavior of the plasma cannot be resolved by LFA. One can make an estimation of the criteria length  $L_{\text{sheath}}$  with BOLSIG+. For a comparative view, we take another example, simulation of nanosecond capillary discharge (nCD) at the pressure of 27.5 mbar as described in [42]. The lower pressure of nCD results in a larger Debye length and  $L_{\text{sheath}}$ . Figure 2 shows the grid size used in the simulation of nCD and nSDBD with the value of  $L_{\text{sheath}}$  for each case.

As has been shown in figure 2, the characteristic length of the sheath defined by equation (11) for nCD and nSDBD is quite different due to the difference in operating pressure. The grid size used in nCD simulation is 10–30  $\mu\text{m}$ , smaller than the characteristic length, meaning that LFA is not applicable for nCD in this work. In contrast, the grid size chosen for nSDBD is larger than the characteristic length, indicating that

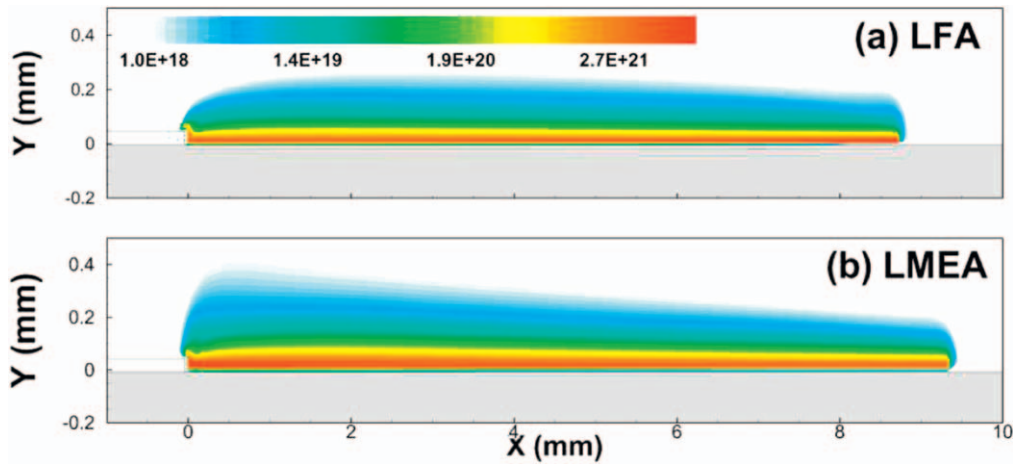


**Figure 3.** Calculation of electron density of an nSDBD at positive polarity with the implementation of (a) LFA and (b) local mean electron energy approximation, units are in  $\text{m}^{-3}$ . Local mean electron energy approximation tends to overestimate the electron temperature if the kinetics scheme is not complete.

the plasma-dielectric sheath region is rather small in nSDBD in atmospheric pressure (or higher). In this work this extremely small region will not be focused upon nor resolved, so that LFA could satisfy the demand of modeling nSDBD with relatively lower computational cost.

Although the LMEA approach is ideally more accurate, it may introduce other problems in the case of the present work: (1) the original numerical scheme for electron flux has not been validated for electron energy flux calculation. Currently, the authors failed to find a very well-defined benchmark case based on LMEA. (2) The electron impact excitation processes considered in the present work are mainly the processes participating in the FGH. The loss of electron energy in excited  $O_2$  and in other  $N_2$  excited species were not taken into consideration, which will lead to overestimation of electron energy and discharge propagation speed. We have conducted a test case by implementing LMEA in the modeling of nSDBD, with the kinetics scheme presented in table 1. As can be seen in figure 3, a comparison between LFA and LMEA shows that there do exist overestimation of the speed of streamer propagation for the case of LMEA, but the difference is small. To be consistent with the previous study [26] and to avoid the issue of validations for LMEA, the authors continue to use the LFA approach for following 2D FGH analysis.

### 3. Results and discussion

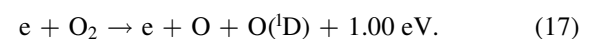
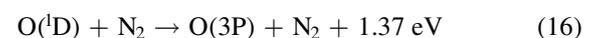
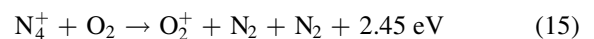
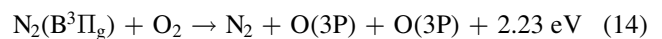
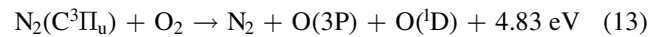
#### 3.1. Dominating reactions contributing to FGH in nSDBD

Paper [18] analyzing the FGH of nanosecond discharges in the range of the reduced electric fields from 150–900 Td classifies the main processes as: (i) quenching of the  $N_2(C^3\Pi_u)$  states by oxygen; (ii) quenching of the  $N_2(B^3\Pi_g)$  states by oxygen; (iii) reactions involving charged particles; (iv) dissociation of  $N_2$  molecules by electron impact followed by quenching of  $N(^2D)$  atoms; (v) quenching of excited  $O(^1D)$  atoms by nitrogen; (vi) dissociation of  $O_2$  molecules by

electron impact; and (vii) quenching of the excited molecules  $N_2(A^3\Sigma_u^+)$  and  $N_2(a^1\Sigma_u^-)$  by oxygen.

Recent publications regarding nSDBD [26, 43, 44] have reported a complex structure of the electric field in the surface streamer, with high fields near the surface, near the electrode, and in the streamer head, and with relatively low fields in the streamer channel. Our calculations show a similar structure of the electric field. Figure 4 presents the electron density and the electric field in the streamer channel averaged along the horizontal line  $25 \mu\text{m}$  above the dielectric surface, and the average is conducted dynamically with the extension of the channel. In the streamer channel, the electron density is one order of magnitude higher in the positive surface streamer than the negative one; on the contrary, the average  $E/N$  in negative surface streamer is about 50 Td higher. For both cases,  $E/N$  is in the range of 50–150 Td when the channel forms. According to [18], the fields in this range correspond to the (i), (ii), (v), and (vi) processes for FGH, while for the higher field region such as the ionization head and cathode region, processes (iii) and (iv) should be more important.

The contribution of individual processes changing in time and space was calculated by the PASSKEY code using the kinetics scheme presented in table 1. The main processes responsible for FGH in nSDBD can be summarized as:



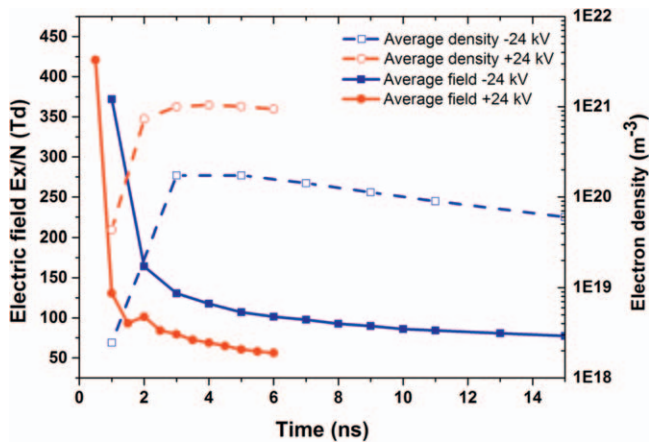


**Figure 4.** The calculated average electric field and electron density in the channel of nSDBD. The values are averaged along the horizontal line  $25 \mu\text{m}$  above the dielectric surface for every time moment.

The reactions mentioned above agree well with the conclusions given in [18]. To further distinguish the contributing reactions to FGH in spatial scale, we plot the contribution from the reactions mentioned above in figures 5(a) and (b) for both polarities. The fraction of energy in each frame is plotted as a fraction of the total energy density spent for the FGH at this point of space. The total energy density is plotted together with the fractions of energies in the bottom of each of the sub-figures. To get the absolute value of heat released in space for each reaction, one should multiply the fraction of energy by the total energy density at each point of space.

The spatial distribution of the released energy shares several features in common for both polarities: (1) energy release from quenching reactions 13 and 14 are dominant in the streamer channel; (2) the contribution of reactions of charged species (15) is extremely small for both cases; (3) total energy density is higher near the electrode and decreases with the distance from the high-voltage electrode for both polarities.

Despite the similarities, the difference in the spatial distribution of the energy release for negative and positive polarity nSDBD is significant. The detailed contribution from the reactions concerning FGH is plotted in figures 6(a) and (b), together with total deposited FGH energy. The fractional contribution of each reaction is taken along a single line probing  $25 \mu\text{m}$  above the dielectric. The following has been found:

- (1) There is higher energy density near the high-voltage electrode. FGH energy density is similar for both polarities near the electrode, but the positive streamer stretches longer and produces the heat in a larger region with lower energy density in the channel—this property can be interesting when the chemical activity of the mixture should be increased without significant hydrodynamic effects, or a large region of gas heating is required. At negative polarity, there is observed a localized region with high energy density near the electrode—this property can be optimal for generation

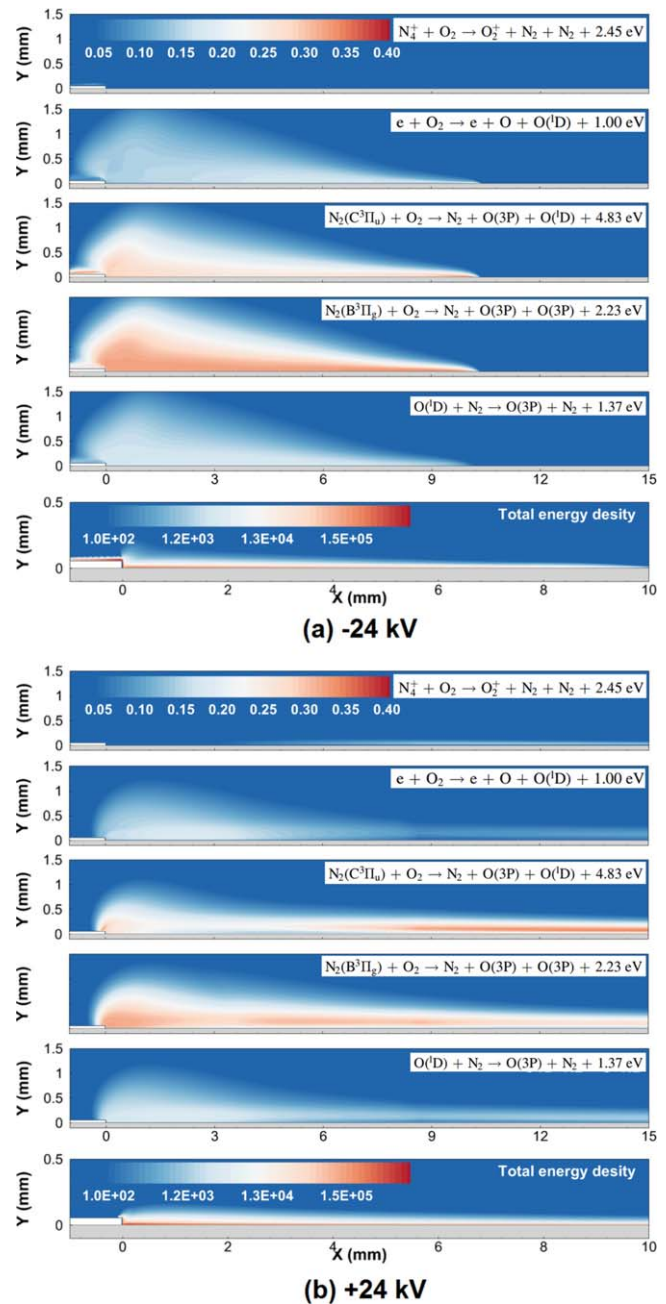


**Figure 5.** The spatial distribution of the fraction of energy from five main reactions contributing to FGH for (a) negative polarity and (b) positive polarity. For each group the last figure gives the distribution of absolute energy density (in unit  $\text{J}/\text{m}^3$ ) released in the gas. Fraction of energy from the main reactions is given as a fraction of the total energy density spent for the FGH at each point of space.

of weak shock waves from the edge of the electrode, or generation of high temperature spot;

- (2) The fractional contribution of individual kinetics is different. In the streamer channel, at negative polarity, the energy fraction is rather uniform across the channel: quenching reactions contribute up to 75% of the energy release, dissociation of  $\text{O}_2$  molecules contributes 20%, and other reactions involving charged species contribute the rest ( $<5\%$ ). For a positive polarity nSDBD, the constitution of energy release changes: at the near

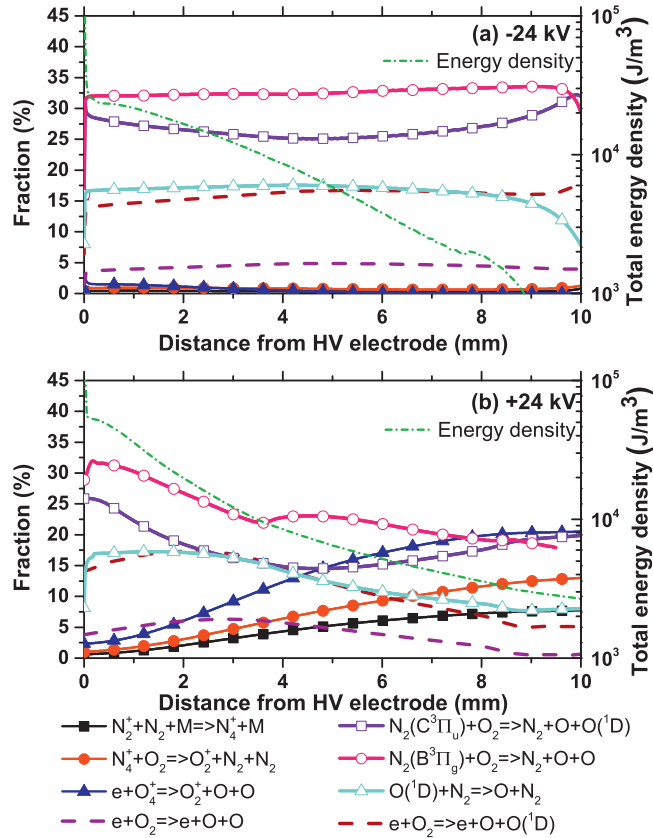


**Figure 6.** Energy density for FGH and the fraction of energy from main reactions contributing to FGH for (a) negative polarity and (b) positive polarity along the line probe  $25 \mu\text{m}$  above the dielectric.

electrode region ( $X < 5 \text{ mm}$ ) quenching and  $\text{O}_2$  dissociation still dominates as in negative polarity, but in the streamer channel far from the high-voltage electrode, the fraction of energy release from reactions of charged species increases from 5%–35%. This change in energy fraction in positive nSDBD is due to the fact that in positive polarity streamer the field in the channel is high near the electrode but low near the ionization head. As the ionization head propagates further away, the field behind the ionization head becomes rather low, resulting in the decrease of excited species production and increase of electron–ion recombination reaction rates, leading to the increase in the fraction of charged species reactions to the total FGH energy fraction.

- (3) At the end of section 2.2, the different approach to heat release in electron–ion recombination reactions was mentioned. It seems that this difference will not bring significant changes to the nSDBD studied in this work, as the electric field is small in the discharge channel. For the negative polarity discharge, the fractional contribution to FGH energy from reactions relating to charged species is smaller than 2%, even with the value used in [25]; so a small increase in FGH is almost invisible in the simulation and cannot be detected in experiments. For a positive polarity, although the fractional contribution of (R21) increases dramatically in the region far from the high-voltage electrode, the

total FGH energy drops by an order of magnitude with the distance. With the rate and energy release used in [25], it is possible to obtain slightly stronger pressure perturbation in the model, but this effect will hardly be seen or validated in the experiments.

It must be noted that in this work a single voltage pulse of 24 kV amplitude was used. The incident and reflected pulses are specifically separated to ensure that there is only one pulse for each measurement; no additional pulses were reflected from the high-voltage generator. In a practical situation, the voltage amplitude can be different and a series of secondary reflections can be observed due to the mismatching of the cable and the generator. The voltage amplitude mainly affects the propagation velocity of the ionization head and the length of the streamer channel. However, once the channel forms, the electric field within the channel is more or less the same. Thus, the mechanisms of the FGH will not change much, and the conclusions mentioned above still work. Once the voltage waveform changes, the discharge dynamics and morphology changes, and the spatial contribution of FGH energy may change. In that case one has to use the measured voltage waveform and the key reactions suggested above to conduct a case-specific study.

The calculated total FGH energy deposition shown in figures 5 and 6, provides us an opportunity to make a comparison with the existing models. In [45] and [46], an analytical model to calculate the total energy density along the plasma channel was proposed assuming the potential inside a streamer body drops almost linearly with distance from the electrode edge. The total energy density is given by equation (18) [46]:

$$W_{\text{total}} \approx \frac{\varepsilon V_0^2}{4\pi d h_d} \left( 1 - \frac{V_{\text{th}}^2}{V_0^2} \right) \left( 1 - \frac{x}{l_s} \right), \quad (18)$$

where  $\varepsilon$  is the relative permittivity,  $V_0$  is the peak voltage,  $d$  is the thickness of dielectric thickness,  $h_d$  is the thickness of the plasma channel,  $V_{\text{th}}$  is the threshold for discharge burning potential of the streamer head, and  $l_s$  is the length of the streamer. This equation provides the total energy deposited to the electrons, and was successfully used in nSDBD cases with lower voltage (14 kV) and short streamers (5 mm for both polarities).

In this work,  $\varepsilon = 4$ ,  $V_0 = 24 \text{ kV}$ ,  $d = 0.45 \text{ mm}$ ,  $V_{\text{th}} = 3 \text{ kV}$ ,  $l_s = 10 \text{ mm}$  for negative polarity and 20 mm for positive polarity. The value of  $h_d$  is not easy to define, as the heating channel, visible channel, and plasma channel are quite different in size. According to the total energy density distribution shown in figure 5, the energy deposition is mainly concentrated in the thin layer of thickness  $0.01 \text{ mm}$ , with the order of  $10^5 \text{ J m}^{-3}$ . Thus, We selected  $0.01 \text{ mm}$  as an approximation for equation (18).

To compare with the analytical results, we plotted together in figure 7 the calculated total and FGH energy density averaged within the  $0\text{--}50 \mu\text{m}$  range above the dielectric. The fractional ratio  $\eta_{\text{total}}$  was evaluated by fitting  $\eta_{\text{total}} W_{\text{total, calculated}}$  with  $W_{\text{FGH, calculated}}$ . For both polarities, the analytical and calculated total energy density are on the same

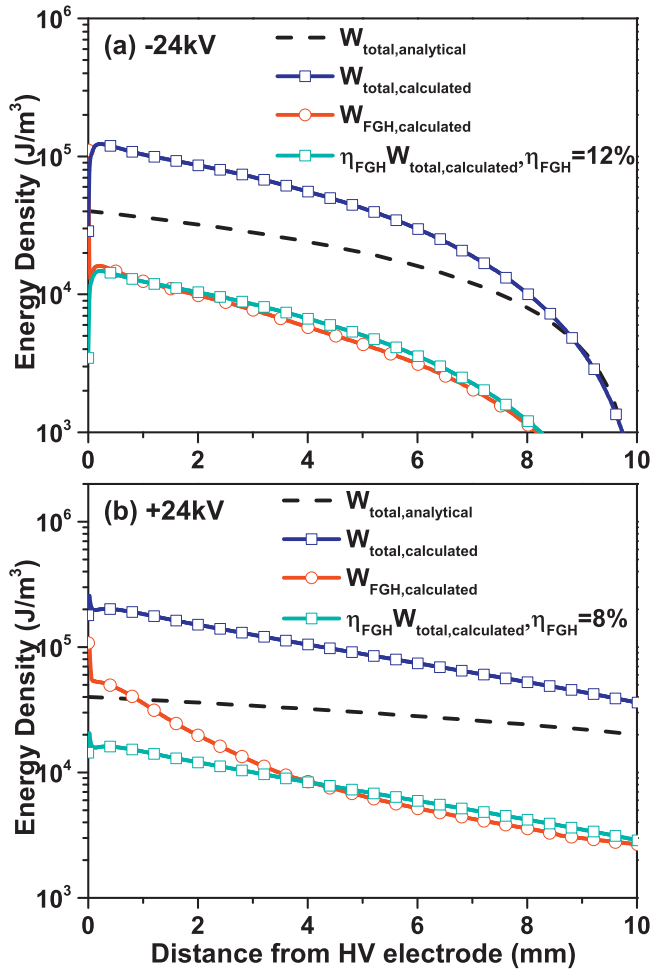


**Figure 7.** Comparison of the density of the deposited FGH energy and analytical results from [46]. (a) negative polarity and (b) positive polarity along the line probe 25  $\mu\text{m}$  above the dielectric. The analytical energy density calculated from [46] was multiplied by the fractional ratio,  $\eta_{total}$ , see the details in the text.

order of magnitude. The analytical model tends to underestimate the energy near the electrode, because the analytical model assumes that energy is released within a rectangular region, while in reality the spatial distribution is triangular. Nevertheless, the analytical model provides a quick insight into the energy distribution with an acceptable error.

It is also interesting to find that for negative polarity, the FGH energy and total energy deposition is proportional in the channel,  $\eta_{total} = 12\%$ . Near the electrode, the existence of a cathode sheath and high electric field lead to the highest  $\eta_{total}$ , about 30%. For positive polarity, the ratio between FGH and total energy deposition is not constant, and ranges from 8% in the channel to 25%–30% near the electrode.

### 3.2. Temperature rise in the channel and near the cathode

The direct consequence of the FGH is the rise of the temperature in the discharge region. The calculated distribution of temperature for the time period from 10 ns in the discharge to 10 000 ns in the afterglow is presented in figure 8(a) for negative polarity and (b) for positive polarity.

To quantify the difference, we probe the temporal temperature evolution near the electrode and in the channel in figure 9, by selecting two points at 25  $\mu\text{m}$  above the dielectric, and 10  $\mu\text{m}$  and 1 mm away from the high-voltage electrode, respectively. For both polarities, a heated channel is observed above the dielectric layer. Near the electrode, the presence of the high field region at negative polarity leads to intensive heating and temperature rise (to 1400 K), while for positive polarity a maximum temperature of 500 K is observed at the edge of electrode. In the channel, the temperature rise at positive polarity is higher (to 500 K) than the temperature rise at negative polarity (to 400 K). It must be noted that in this work the energy release from vibrational relaxation which is significant in the time scale of  $\mu\text{s}$  is not calculated, thus the temperature at 10 000 ns should be underestimated. The temperature at the cathode region is also underestimated due to the neglect of ion current, as has been mentioned in section 2.2.

A temperature rise of about 40 K in the channel (1 mm away from the high-voltage electrode) during the first 10 ns can be observed in the sub-figure in figure 9. This is in good agreement with the results of the experimental observation of [47], where the experimental measurements of the temperature of nSDBD using the same voltage waveform but with 40–50 kV amplitude resulted in the temperature rise of 30–70 K during the first 10 ns.

The generation and propagation of compression waves in nanosecond SDBDs is one of the most typical nSDBD phenomena observed both in experiments and simulations [6, 48–50]. A recent study of hydrodynamic responses of nSDBD [26] has revealed that in the formation stage of compressive waves, for both polarities, a strong perturbation of pressure is observed along the dielectric surface (‘wave 1’ hereinafter) and at the edge of the exposed electrode due to fast and local heat release in chemical reactions (‘wave 2’). The waves propagate with approximately constant slightly supersonic velocity at  $t < 2\text{--}2.5 \mu\text{s}$  and then slow down.

For negative polarity nSDBD, waves 1 and 2 are well distinguished; for positive polarity, wave 1 is more uniformly distributed above the dielectric. An interesting fact is that for negative polarity, increased energy release in the near-cathode region is clearly seen (‘wave 3’). Numerical simulation makes it possible to analyze the formation of waves 1, 2, and 3 relative to the FGH. A probe at the starting point of each wave (marked with the black points in figure 8) results in figure 10, in which the source reactions and their contributions to the formation of each wave are plotted and compared.

Figure 10(a) demonstrates the fractional contribution for each wave at negative polarity. The results show that different appearances of wave 3 and waves 1 and 2 correlate with the quenching of  $\text{N}_2(\text{C}^3\Pi_u)$  level: at negative polarity,  $\text{N}_2(\text{C}^3\Pi_u)$  is produced in the thin layer over the high-voltage electrode; as a result, the flat wave 3 starts from the electrode. Another important issue is that the FGH in both the streamer channel and the near-cathode region is caused mainly by quenching of excited nitrogen molecules rather than by reactions related to charged species. Figure 10(b) provides a direct comparison between the pressure waves generated at negative and

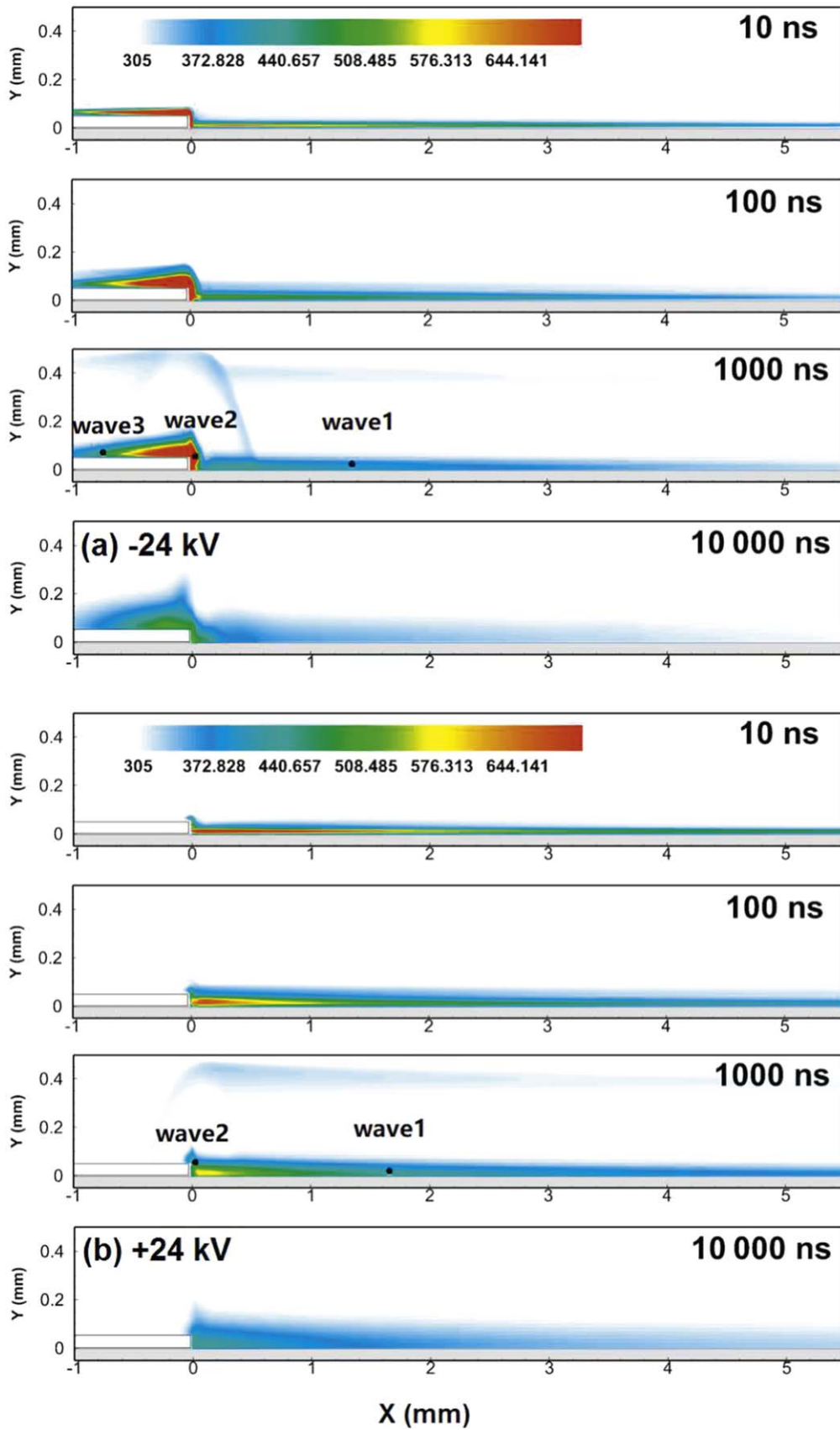


**Figure 8.** The evolution of the calculated temperature distributions (in K) from 10–10 000 ns for (a) negative polarity and (b) positive polarity discharge.

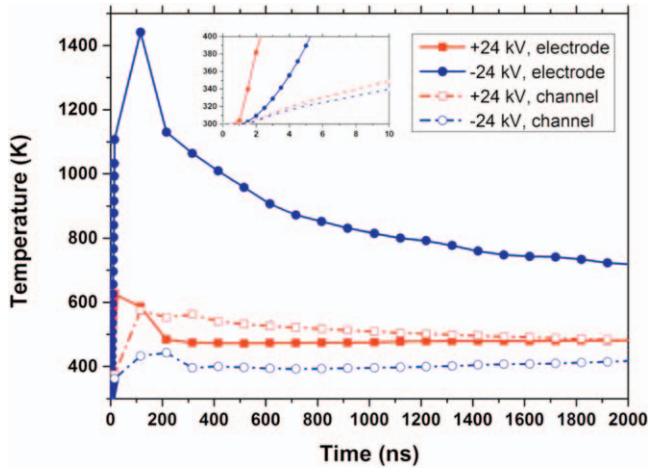


**Figure 9.** The temporal evolution of temperature during and after the discharge for discharges of both polarities. The solid scatter line indicates the temperature in the vicinity of the high-voltage electrode ( $10\ \mu\text{m}$  from the high-voltage electrode), and the empty scatter line indicates the temperature in the streamer channel (1 mm from the high-voltage electrode). Red lines and square symbols indicate the data for positive polarity; blue lines and circles—for negative polarity. The sub-figure is zoomed for the time period of 0–10 ns.

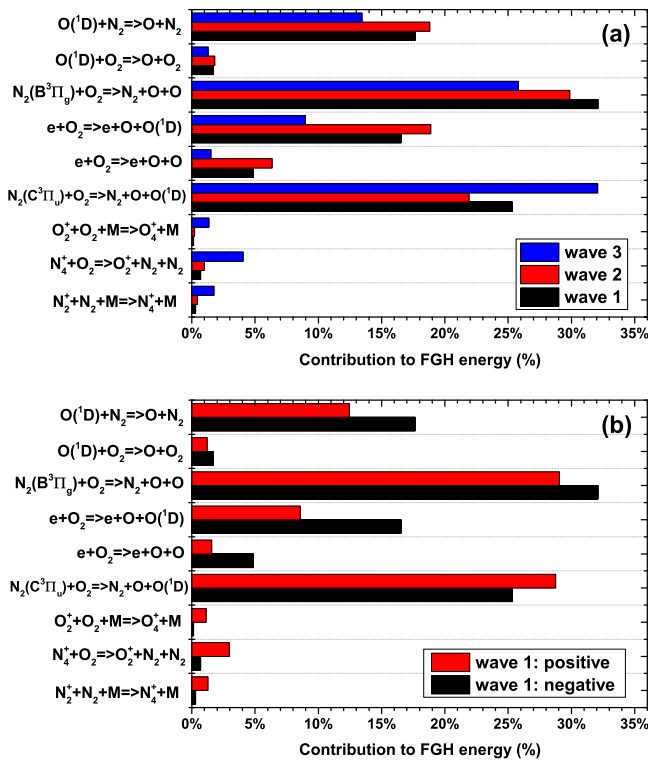


**Figure 10.** The constitution of the energy for FGh. (a) the contribution fraction responsible for the generation of different compressive waves in negative polarity discharge; (b) the contribution fraction in wave 1 for both polarities.

positive polarities: despite the different morphologies and electric fields for different polarities, the contribution to FGh energy from individual reactions is rather similar.

Taking into account that there exist a few numerical studies of FGh in nanosecond pulsed discharges at different

geometries, it is interesting to compare them with the present results. Two typical studies are selected for this comparison: a pin-to-plane discharge case [23, 24] and a pin-to-pin discharge [20]. In both cases, the detailed voltage-current characteristics, the total energy deposition, the fraction ratio of the FGh energy to the total deposited energy, and the spatial-temporal temperature evolution are presented and discussed. Direct comparisons of FGh parameters for pin-to-plane discharge, pin-to-pin discharge, and nSDBD under both polarities are listed in table 2.

In table 2,  $U_{\text{max}}$ , FWHM, voltage rising rate,  $T_{\text{max}}$ , and  $T_{\text{channel}}$  are taken from original papers directly. The heating volumes  $V_{\text{heat}}$  are calculated according to the heated region ( $\Delta T > 50\text{K}$ ),  $W_{\text{total}}$  is calculated based on the voltage-current profiles of each case (if available).  $\eta_{\text{total}}$  is calculated for each case. For the pin-plane case,  $W_{\text{FGH}}$  was calculated from existing figures (total gas heating energy minus energy stored in vibrational states of  $N_2$ ) in [24], thus  $\eta_{\text{total}} = W_{\text{FGH}}/W_{\text{total}}$ . For the pin-pin case, the detailed kinetics were not included, so FGh energy was directly calculated through assumed  $\eta_{\text{total}}$  according to [18, 25]. For the nSDBD cases,  $\eta_{\text{total}}$  has been discussed based on figure 7.

It is shown in table 2 that the applied voltage varies. The pin-to-plane case was conducted in a 13 mm gap. It has the same peak voltage as the nSDBD case, but much longer FWHM and slower rising time, resulting in low  $W_{\text{total}}$  and  $W_{\text{FGH}}$ . The pin-to-pin case with  $T_{\text{base}} = 1000\text{K}$ , in contrast, is conducted by a shorter and lower voltage within a 2.5 mm gap. The discharge enters into the spark stage, resulting in the highest  $W_{\text{total}}$ , and the high field in the spark stage makes  $\eta_{\text{total}}$  possible to be the highest among all three cases. nSDBD heats the largest region, and it increases the gas temperature to almost the same magnitude in comparison with other cases at  $T_{\text{base}} = 300\text{K}$ .

Conclusions can be drawn from table 2 and the above discussion that SDBD driven by a nanosecond voltage pulse with short rising time can achieve a comparable temperature increase with pin-plane and pin-pin discharges through FGh. Also we have to be aware that the  $\Delta T_{\text{max}} = 1100\text{K}$  obtained for nSDBD is available only in a thin sheath region (about 0.01 mm within an high-voltage electrode), whereas the maximum temperature increase in the pin-plane and pin-pin cases appears within 0.5 mm around the pin electrode.

## 4. Conclusions

FGh has been analyzed for an nSDBD by a 2D model. The parallel PASSKey code validated by measurements conducted at the same experimental conditions [26] as in the present paper was used. The LFA was used instead of LMEA to have a minimum set of kinetics solved for 2D modeling. The main processes contributing to the FGh in nSDBD were quantitatively analyzed. The fractional contribution of individual reactions varies with the distance from the high-voltage electrode and polarity. The quenching reactions were found to be the main source of FGh energy release and the

**Table 2.** List of FGH cases at different geometries.

	Pin-to-plane	Pin-to-pin	Pin-to-pin	nSDBD–	nSDBD+
Ref.	[23, 24]	[20]	[20]	[26]	[26]
$T_{\text{base}}$ , K	300	300	1000	300	300
$U_{\text{max}}$ , kV	24	5	5	24	24
FWHM, ns	400	8	8	20	20
Rising rate, kV/ns	0.52	2.5	2.5	12	12
$V_{\text{heat}}$ , $10^{-3}\text{cm}^3$	0.59	0.49	1.96	2.03	4.20
$W_{\text{total}}$ , mJ	0.11	...	45.0	1.82	3.01
$W_{\text{FGH}}$ , mJ	<0.02	...	...	...	...
$\eta_{\text{total}}$	<18%	15%–60%	15%–60%	12%–30%	8%–30%
$\Delta T_{\text{max}}$ , K	900	500	1000	1100	300
$\Delta T_{\text{channel}}$ , K	20	200	875	100	200

main reason for the generation of hydrodynamic perturbations at both polarities.

The total and FGH energy density are obtained. The fraction of energy transferred from total energy to FGH energy ranges from 8%–30%, depending on polarities and locations. FGH energy density is higher near the electrode and decreases with the distance from the high-voltage electrode at both polarities. For both polarities, the FGH energy density reaches  $10^4$ – $10^5 \text{ J m}^{-3}$  (that is,  $10^{12}$ – $10^{13} \text{ W m}^{-3}$  in power density) when the distance from the high-voltage electrode is smaller than 4 mm. With the distance increase, the FGH energy decreases dramatically at negative polarity. The heated region at positive polarity is larger with a relatively lower temperature; for negative polarity a stronger heating can be observed near the electrode due to the higher field near the cathode.

FGH leads to the temperature rise on a sub-microsecond scale. For both polarities, the plasma channel heats the air above the dielectric. Near the electrode edge, the temperature at negative polarity can be as high as 1400 K near the cathode region, while for positive polarity the maximum temperature is about 500 K. In the streamer channel, temperature rise at positive polarity is 100–200 K higher than that at negative polarity. Compared with nanosecond pin-to-pin and pin-to-plate discharges, nSDBD can affect a larger region and achieve a comparable temperature increase through FGH.

## Acknowledgments

The work was partially supported by the French National Agency, ANR (ASPEN Project, ANR-16-CE30-0004-01), by LabEx Plas@Par, as part of the ‘Investments for the Future’ French National Program ANR-11-IDEX-0004-02, and by the Linked International Laboratory LIA KaPPA (France–Russia). The authors are grateful to Dr Nikolay A Popov (Moscow State University) for fruitful scientific discussions.

## ORCID iDs

Yifei Zhu  <https://orcid.org/0000-0001-8989-0051>

## References

- [1] Roth J R, Sherman D M and Wilkinson S P 2000 Electrohydrodynamic flow control with a glow-discharge surface plasma *AIAA J.* **38** 1166–72
- [2] Roth J R 2003 Aerodynamic flow acceleration using paraelectric and peristaltic electrohydrodynamic effects of a one atmosphere uniform glow discharge plasma *Phys. Plasmas* **10** 2117–26
- [3] Enloe C, McLaughlin T E, VanDyken R D, Kachner K, Jumper E J, Corke T C, Post M and Haddad O 2004 Mechanisms and responses of a single dielectric barrier plasma actuator: geometric effects *AIAA J.* **42** 595–604
- [4] Enloe C, McHarg M and McLaughlin T E 2008 Time-correlated force production measurements of the dielectric barrier discharge plasma aerodynamic actuator *J. Appl. Phys.* **103** 073302
- [5] Opaits D, Roupasov D, Starikovskaia S, Starikovskii A Y, Zavialov I and Saddoughi S 2005 Plasma control of boundary layer using low-temperature non-equilibrium plasma of gas discharge *43rd AIAA Aerospace Sciences Meeting and Exhibit AIAA* 2005-1180
- [6] Starikovskii A Y, Nikipelov A, Nudnova M and Roupasov D 2009 SDBD plasma actuator with nanosecond pulse-periodic discharge *Plasma Sources Sci. Technol.* **18** 034015
- [7] Leonov S, Opaits D, Miles R and Soloviev V 2010 Time-resolved measurements of plasma-induced momentum in air and nitrogen under dielectric barrier discharge actuation *Phys. Plasmas* **17** 113505
- [8] Rethmel C, Little J, Takashima K, Sinha A, Adamovich I and Samimy M 2011 Flow separation control using nanosecond pulse driven DBD plasma actuators *Int. J. Flow Control* **3** 213
- [9] Bisek N J, Poggie J, Nishihara M and Adamovich I 2014 Hypersonic flow over a cylinder with a nanosecond pulse electrical discharge *J. Thermophys. Heat Transfer* **28** 18–26
- [10] Bayoda K, Benard N and Moreau E 2015 Nanosecond pulsed sliding dielectric barrier discharge plasma actuator for airflow control: electrical, optical, and mechanical characteristics *J. Appl. Phys.* **118** 063301
- [11] Leonov S B, Adamovich I V and Soloviev V R 2016 Dynamics of near-surface electric discharges and mechanisms of their interaction with the airflow *Plasma Sources Sci. Technol.* **25** 063001
- [12] Starikovskaia S, Allegraud K, Guaitella O, Kosarev I, Mintusov E, Pendleton S J, Popov N, Sagulenko P and Rousseau A 2010 Surface discharges: possible applications for plasma-assisted ignition and electric field measurements *48th AIAA Aerospace Sciences Meeting including the New Horizons Forum and Aerospace Exposition*

- [13] Liu Y, Kolbakir C, Hu H and Hu H 2018 A comparison study on the thermal effects in DBD plasma actuation and electrical heating for aircraft icing mitigation *Int. J. Heat Mass Transfer* **124** 319–30
- [14] Zhou W, Liu Y, Hu H, Hu H and Meng X 2018 Utilization of thermal effect induced by plasma generation for aircraft icing mitigation *AIAA J.* **56** 1097–104
- [15] Kolbakir C, Liu Y, Hu H, Starikovskiy A and Miles R B 2018 An experimental investigation on the thermal effects of NS-DBD and AC-DBD plasma actuators for aircraft icing mitigation *2018 AIAA Aerospace Sciences Meeting* 0164
- [16] Rusterholtz D, Pai D, Stancu G, Lacoste D and Laux C 2012 Ultrafast heating in nanosecond discharges in atmospheric pressure air *50th AIAA Aerospace Sciences Meeting including the New Horizons Forum and Aerospace Exposition*
- [17] Lo A, Cessou A, Boubert P and Vervisch P 2014 Space and time analysis of the nanosecond scale discharges in atmospheric pressure air: I. Gas temperature and vibrational distribution function of N<sub>2</sub> and O<sub>2</sub> *J. Phys. D: Appl. Phys.* **47** 115201
- [18] Popov N 2011 Fast gas heating in a nitrogen-oxygen discharge plasma: I. Kinetic mechanism *J. Phys. D: Appl. Phys.* **44** 285201
- [19] Nudnova M, Aleksandrov N and Starikovskii A Y 2010 Influence of the voltage polarity on the properties of a nanosecond surface barrier discharge in atmospheric-pressure air *Plasma Phys. Rep.* **36** 90–8
- [20] Tholin F and Bourdon A 2013 Simulation of the hydrodynamic expansion following a nanosecond pulsed spark discharge in air at atmospheric pressure *J. Phys. D: Appl. Phys.* **46** 365205
- [21] Tholin F 2012 Numerical simulation of nanosecond repetitively pulsed discharges in air at atmospheric pressure: Application to plasma-assisted combustion *PhD Thesis* Ecole Centrale Paris
- [22] Tholin F, Lacoste D A and Bourdon A 2014 Influence of fast-heating processes and O atom production by a nanosecond spark discharge on the ignition of a lean H<sub>2</sub>-air premixed flame *Combust. Flame* **161** 1235–46
- [23] Komuro A, Ono R and Oda T 2013 Effects of pulse voltage rise rate on velocity, diameter and radical production of an atmospheric-pressure streamer discharge *Plasma Sources Sci. Technol.* **22** 045002
- [24] Komuro A and Ono R 2014 Two-dimensional simulation of fast gas heating in an atmospheric pressure streamer discharge and humidity effects *J. Phys. D: Appl. Phys.* **47** 155202
- [25] Aleksandrov N, Kindysheva S, Nudnova M and Starikovskiy A Y 2010 Mechanism of ultra-fast heating in a non-equilibrium weakly ionized air discharge plasma in high electric fields *J. Phys. D: Appl. Phys.* **43** 255201
- [26] Zhu Y, Shcherbanev S, Baron B and Starikovskaia S 2017 Nanosecond surface dielectric barrier discharge in atmospheric pressure air: I. Measurements and 2D modeling of morphology, propagation and hydrodynamic perturbations *Plasma Sources Sci. Technol.* **26** 125004
- [27] Zhelezniak M, Mnatsakanian A K and Szykh S V 1982 Photoionization of nitrogen and oxygen mixtures by radiation from a gas discharge *High Temp. Sci.* **20** 423–8
- [28] Bourdon A, Pasko V, Liu N, Célestin S, Ségur P and Marode E 2007 Efficient models for photoionization produced by non-thermal gas discharges in air based on radiative transfer and the Helmholtz equations *Plasma Sources Sci. Technol.* **16** 656
- [29] Luque A, Ebert U, Montijn C and Hundsdoerfer W 2007 Photoionization in negative streamers: fast computations and two propagation modes *Appl. Phys. Lett.* **90** 081501
- [30] Pancheshnyi S, Nudnova M and Starikovskii A 2005 Development of a cathode-directed streamer discharge in air at different pressures: experiment and comparison with direct numerical simulation *Phys. Rev. E* **71** 016407
- [31] Capitelli M, Ferreira C M, Gordiets B F and Osipov A I 2001 *Plasma Kinetics in Atmospheric Gases* 31 (Berlin: Springer Science & Business Media)
- [32] Phelps A and Pitchford L 1985 Anisotropic scattering of electrons by N<sub>2</sub> and its effect on electron transport *Phys. Rev. A* **31** 2932
- [33] Lawton S and Phelps A 1978 Excitation of the  $b^1\Sigma_g^+$  state of O<sub>2</sub> by low energy electrons *J. Chem. Phys.* **69** 1055–68
- [34] Kossyi I, Kostinsky A Y, Matveyev A and Silakov V 1992 Kinetic scheme of the non-equilibrium discharge in nitrogen-oxygen mixtures *Plasma Sources Sci. Technol.* **1** 207
- [35] Hagelaar G and Pitchford L 2005 Solving the Boltzmann equation to obtain electron transport coefficients and rate coefficients for fluid models *Plasma Sources Sci. Technol.* **14** 722
- [36] Naidis G 1997 Effects of nonlocality on the dynamics of streamers in positive corona discharges *Tech. Phys. Lett.* **23** 493–4
- [37] Aleksandrov N and Kochetov I 1996 Electron rate coefficients in gases under non-uniform field and electron density conditions *J. Phys. D: Appl. Phys.* **29** 1476
- [38] Li C, Brok W, Ebert U and Van der Mullen J 2007 Deviations from the local field approximation in negative streamer heads *J. Appl. Phys.* **101** 123305
- [39] Chanrion O and Neubert T 2008 A PIC-MCC code for simulation of streamer propagation in air *J. Comput. Phys.* **227** 7222–45
- [40] Liu N and Pasko V P 2004 Effects of photoionization on propagation and branching of positive and negative streamers in sprites *J. Geophys. Res.: Space Phys.* **109** A04301
- [41] Soloviev V and Krivtsov V 2009 Surface barrier discharge modelling for aerodynamic applications *J. Phys. D: Appl. Phys.* **42** 125208
- [42] Klochko A V, Starikovskaia S M, Xiong Z and Kushner M J 2014 Investigation of capillary nanosecond discharges in air at moderate pressure: comparison of experiments and 2D numerical modelling *J. Phys. D: Appl. Phys.* **47** 365202
- [43] Stepanyan S, Soloviev V and Starikovskaia S 2014 An electric field in nanosecond surface dielectric barrier discharge at different polarities of the high voltage pulse: spectroscopy measurements and numerical modeling *J. Phys. D: Appl. Phys.* **47** 485201
- [44] Babaeva N Y, Tereshonok D V and Naidis G V 2016 Fluid and hybrid modeling of nanosecond surface discharges: effect of polarity and secondary electrons emission *Plasma Sources Sci. Technol.* **25** 044008
- [45] Anokhin E, Kuzmenko D, Kindysheva S, Soloviev V and Aleksandrov N 2015 Ignition of hydrocarbon: air mixtures by a nanosecond surface dielectric barrier discharge *Plasma Sources Sci. Technol.* **24** 045014
- [46] Soloviev V and Krivtsov V 2015 Analytical and numerical estimation of the body force and heat sources generated by the surface dielectric barrier discharge powered by alternating voltage *EUCASS 2015 VI European Conf. for Aeronautics and Space Science*
- [47] Shcherbanev S, Stepanyan S, Popov N and Starikovskaia S 2015 Dielectric barrier discharge for multi-point plasma-assisted ignition at high pressures *Phil. Trans. R. Soc. A* **373** 20140342
- [48] Unfer T and Boeuf J 2009 Modelling of a nanosecond surface discharge actuator *J. Phys. D: Appl. Phys.* **42** 194017
- [49] Takashima K, Zuzeeck Y, Lempert W R and Adamovich I V 2011 Characterization of a surface dielectric barrier

- discharge plasma sustained by repetitive nanosecond pulses *Plasma Sources Sci. Technol.* **20** 055009
- [50] Zhu Y, Wu Y, Cui W, Li Y and Jia M 2013 Modelling of plasma aerodynamic actuation driven by nanosecond SDBD discharge *J. Phys. D: Appl. Phys.* **46** 355205